AGU PUBLICATIONS

Geochemistry, Geophysics, Geosystems

RESEARCH ARTICLE
10.1002/2014GC005709

Special Section:
The Lithosphere-asthenosphere System

The electrical structure of the central Pacific upper mantle constrained by the NoMelt experiment

Emily Sarafian[1], Rob. L. Evans[2], John A. Collins[2], Jimmy Elsenbeck[2], Glenn A. Gaetani[2], James B. Gaherty[3], Greg Hirth[4], and Daniel Lizarralde[2]

[1]MIT/WHOI Joint Program, Woods Hole, Massachusetts, USA, [2]Department of Geology and Geophysics, Woods Hole Oceanographic Institution, Woods Hole, Massachusetts, USA, [3]Lamont-Doherty Earth Observatory of Columbia University, Palisades, New York, USA, [4]Geological Sciences Department, Brown University, Providence, Rhode Island, USA

Abstract The NoMelt experiment imaged the mantle beneath 70 Ma Pacific seafloor with the aim of understanding the transition from the lithosphere to the underlying convecting asthenosphere. Seafloor magnetotelluric data from four stations were analyzed using 2-D regularized inverse modeling. The preferred electrical model for the region contains an 80 km thick resistive ($>10^3$ Ωm) lithosphere with a less resistive (~50 Ωm) underlying asthenosphere. The preferred model is isotropic and lacks a highly conductive ($\leq$10 Ωm) layer under the resistive lithosphere that would be indicative of partial melt. We first examine temperature profiles that are consistent with the observed conductivity profile. Our profile is consistent with a mantle adiabat ranging from 0.3 to 0.5°C/km. A choice of the higher adiabatic gradient means that the observed conductivity can be explained solely by temperature. In contrast, a 0.3°C/km adiabat requires an additional mechanism to explain the observed conductivity profile. Of the plausible mechanisms, H_2O, in the form of hydrogen dissolved in olivine, is the most likely explanation for this additional conductivity. Our profile is consistent with a mostly dry lithosphere to 80 km depth, with bulk H_2O contents increasing to between 25 and 400 ppm by weight in the asthenosphere with specific values dependent on the choice of laboratory data set of hydrous olivine conductivity and the value of mantle oxygen fugacity. The estimated H_2O contents support the theory that the rheological lithosphere is a result of dehydration during melting at a mid-ocean ridge with the asthenosphere remaining partially hydrated and weakened as a result.

Key Points:
- MT data in the Pacific constrain lithospheric thickness and mantle structure
- The observed conductivity is used to estimate asthenospheric water content
- The electrical LAB lacks a highly conductive layer indicative of melt

Correspondence to:
E. Sarafian,
etursack@whoi.edu

Citation:
Sarafian, E., R. L. Evans, J. A. Collins, J. Elsenbeck, G. A. Gaetani, J. B. Gaherty, G. Hirth, and D. Lizarralde (2015), The electrical structure of the central Pacific upper mantle constrained by the NoMelt experiment, *Geochem. Geophys. Geosyst.*, *16*, 1115–1132, doi:10.1002/2014GC005709.

Received 30 DEC 2014
Accepted 25 MAR 2015
Accepted article online 28 MAR 2015
Published online 18 APR 2015

1. Introduction

The theory of plate tectonics divides Earth's upper mantle into rigid lithospheric plates that move over a weaker, convecting asthenosphere. The transition from a rigid plate to the underlying asthenosphere occurs at variable depths in the mantle depending on tectonic setting [*Plomerová et al.*, 2002] and is a critical boundary in determining plate behavior [*Bunge et al.*, 1996; *Richards et al.*, 2002; *Hoink and Lenardic*, 2008]. Researchers have long debated the rheology of the upper mantle and the lithosphere-asthenosphere boundary (LAB), particularly the mechanisms needed to weaken the asthenosphere to account for observed plate behavior. Early interpretations of geophysical measurements included the presence of melt in the upper oceanic asthenosphere [e.g., *Anderson and Sammis*, 1970; *Anderson and Spetzler*, 1970; *Lambert and Wyllie*, 1970]. New geophysical models along with a host of recent laboratory conductivity measurements have added to the debate, particularly over whether the uppermost asthenosphere immediately below the LAB is weakened as a result of the presence of hydrogen [e.g., *Gaherty et al.*, 1996; *Hirth and Kohlstedt*, 1996; *Phipps Morgan*, 1997; *Karato and Jung*, 1998], melt [*Anderson and Sammis*, 1970; *Anderson and Spetzler*, 1970; *Lambert and Wyllie*, 1970; *Kawakatsu et al.*, 2009; *Schmerr*, 2012] or a combination of the two.

In the oceans, the evolution of the mantle is arguably more straightforward than in continental settings as lithospheric plates cool and grow as they move away from mid-ocean ridges, yet the difficulty of making detailed localized measurements in the oceans means that we still know surprisingly little of its structure and evolution. Decades of global seismic studies provide some insight into the evolution of the oceanic lithosphere [e.g., *Ritzwoller et al.*, 2004; *Nettles and Dziewonski*, 2008; *Priestley and McKenzie*, 2006]. However, such analyses have generally used data sets that span ocean basins and thus do not well constrain critical, more subtle features that are diagnostic of composition and evolutionary processes. Constraints on the depth dependence of shear-velocity structure in the oceanic lithosphere and across the LAB come primarily

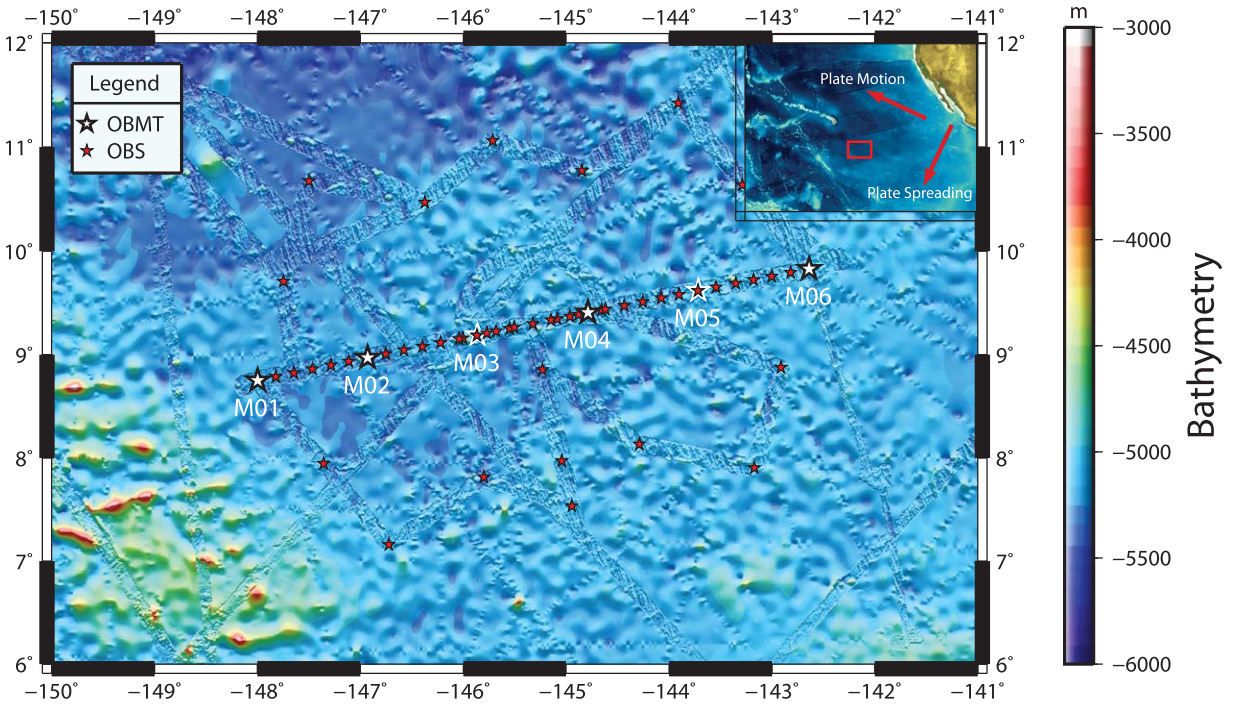

Figure 1. Shown is the region of the NoMelt experiment. White stars indicate MT stations 1–6 along a linear array—filled stars are stations that provided useable data, unfilled stars were not used. Red stars indicate the locations of seismic stations. Figure insert shows the location of the region and the current plate motion and the plate spreading direction used during inversion.

from regional surface and body-wave studies [*Nishimura and Forsyth*, 1989; *Gaherty et al*., 1996; *Gu et al*., 2005; *Tan and Helmberger*, 2007], studies of mantle reflectivity from old Pacific lithosphere [*Revenaugh and Jordan*, 1991; *Collins et al*., 2002; *Bagley and Revenaugh*, 2008], receiver function studies [*Rychert and Shearer*, 2009; *Kawakatsu et al*., 2009], as well as from analysis of seismic phase SS precursors [*Schmerr*, 2012]. These studies showed that the transition from the lithosphere to the asthenosphere is complex with multiple seismic discontinuities observed within the transitional region at various oceanic plate ages. Observations include a seismic discontinuity mapped by SS waveforms, the depth of which increases with plate age [*Rychert and Shearer*, 2011]. This SS Lithospheric Profiling (SSLIP) reflector has been interpreted as the LAB with its depth dependent on a critical temperature of ∼950°C in the uppermost asthenosphere. Observations from the western Pacific and the Philippine Sea, over a range of seafloor ages (∼40–130 Ma), further identify a sharp LAB with the suggestion that the underlying asthenosphere contains some degree of partial melt [*Kawakatsu et al*., 2009]. Another observed seismic feature is an abrupt drop in seismic velocity (the so-called G discontinuity) at depths of ∼70–80 km independent of plate age, which is too sharp to be thermal in origin [e.g., *Bagley and Revenaugh*, 2008], and has been interpreted variously in terms of partial melt, decreased grain size, a change in anisotropy, and/or the presence of a hydrous asthenosphere. A self-consistent quantitative explanation for the observed LAB structure has yet to be determined, leaving the relationship between the G discontinuity and the LAB unclear. Recent Pacific basin-wide observations suggest that the LAB is a thermal boundary whereas the G discontinuity remains more elusive and is related to changes in mantle seismic anisotropy either due to a compositional or dynamical variation, such as hydration or melt [*Rychert et al*., 2012; *Beghein et al*., 2014].

The NoMelt experiment set out to image the structure of intermediate-age oceanic upper mantle in order to better understand the mechanisms responsible for the transition between the lithosphere and asthenosphere. The experiment took place on 70 Ma Pacific seafloor between the Clarion and Clipperton fracture zones (Figure 1). At this age, the thermal lithosphere is expected to be deeper than the G discontinuity and to have overgrown shallow conductive features seen elsewhere [e.g., *Evans et al*., 2005; *Naif et al*., 2013]. A combination of seismic and magnetotelluric (MT) techniques were used to image the upper mantle. This paper focuses on the inversion and interpretation of the seafloor MT data collected. MT maps the

subsurface conductivity structure, which is sensitive to temperature, amount of dissolved hydrogen, and interconnected conductors such as melt or fluid. As a result, electromagnetic methods offer considerable insight into the debate over the nature of the LAB transition [e.g., *Eaton et al*., 2009]. Two-dimensional isotropic and anisotropic inversion techniques were used to obtain the electrical structure of the upper mantle. The resulting electrical model is then averaged into a 1-D profile and compared with recent laboratory data to determine the influence of temperature, H_2O content, and the possibility of partial melt through the LAB and in the uppermost asthenosphere.

1.1. Mantle Conductivity: A Summary

Mantle conductivity models, particularly those related to H_2O and partial melting, have been evolving over the last few years due to progress in laboratory conductivity measurements. In this paper, two of the most recent hydrous olivine conductivity models and a recent melt conductivity model are used to evaluate the dominant mechanism operative in the study area. This section provides a brief overview of the models used for interpretation.

Mantle nominally anhydrous minerals (NAMs), such as olivine, orthopyroxene (opx), clinopyroxene (cpx), and spinel or garnet, can accommodate various amounts of dissolved H_2O (hydrogen) at upper mantle conditions. In the H_2O model for the LAB, a dehydrated lithosphere sits above a more hydrous asthenosphere of lower viscosity [e.g., *Hirth and Kohlstedt*, 1996]. The increase in mantle H_2O content may influence the seismic velocity of the mantle rocks via its influence on seismic attenuation [e.g., *Karato and Jung*, 1998; *Karato*, 2006; *Olugboji et al*., 2013] consistent with the observed LAB seismic properties, though recent work suggests that the effect of H_2O may not be enough to account for rheological changes [*Fei et al*., 2013]. In addition, dissolved H_2O can enhance the electrical conductivity of mantle minerals [*Wang et al*., 2006; *Yoshino et al*., 2009; *Poe et al*., 2010; *Dai and Karato*, 2014], yet there is still considerable disagreement between the various laboratories reporting conductivity measurements on hydrous olivine (see discussion in *Evans* [2012] and *Jones et al*. [2012]). A recent analysis has attempted to reconcile the published data with a reanalysis of all data sets resulting in a single "unified hydrous olivine" model (UHO) [*Gardes et al*., 2014]. Nonetheless, subsequent studies have reopened the controversy, with results apparently suggesting that two conduction mechanisms are operative, one at low temperatures expected in the lithosphere and one at asthenospheric temperatures [*Dai and Karato*, 2014]. At higher temperatures, conductivity is enhanced by dissolved H_2O to a greater degree than predicted by the UHO model. Also at issue is whether conductivity in hydrous olivine is anisotropic, with higher conductivity along the *a* axis, as expected from laboratory measurements of hydrogen diffusion [*Mackwell and Kohlstedt*, 1990; *Kohlstedt and Mackwell*, 1998]. Some published conductivity data [e.g., *Yoshino et al*., 2006] do not support a model in which a damp mantle with an *a* axis aligned olivine fabric would exhibit electrical anisotropy as suggested by *Evans et al*. [2005], but again, more recent data appear to place this model back into contention [*Dai and Karato*, 2014].

Another mechanism to enhance conductivity is partial melt. *Shankland and Waff* [1977] showed that silicate melt is a semiconductor with conductivity dependent on temperature and weakly on pressure. Partial melts of mantle materials have conductivities in the range of 1–10 S/m, substantially higher than anhydrous subsolidus olivine, although the conductivity of a particular melt depends on composition (H_2O and CO_2 in particular) [*Yoshino et al*., 2012; *Sifre et al*., 2014], temperature, and pressure [*Roberts and Tyburczy*, 1999; *Toffelmier and Tyburczy*, 2007; *Yoshino et al*., 2012; *Sifre et al*., 2014]. For example, at constant pressure the addition of H_2O to melt promotes an increase in conductivity [e.g., *Ni et al*., 2011; *Pommier et al*., 2008]. Furthermore, for a given temperature and melt fraction, order of magnitude variations in electrical conductivity can also result from relatively minor changes in the melt interconnection geometry or texture [*Schmeling*, 1986; *Roberts and Tyburczy*, 1999; *ten Grotenhuis et al*., 2005]. Other effects on melt conductivity are Na content, which can increase conductivity at the incipient stages of melting [*Pommier and Garnero*, 2014] and CO_2 content, which at the very early stages of melting can dramatically increase conductivity [*Sifre et al*., 2014]. The above studies indicate the effect of melt on conductivity is greater than previously thought when interpreting field results [*Pommier and Garnero*, 2014; *Sifre et al*., 2014]. This means that MT is in fact able to detect very small silicate melt fractions (typically on the order of 0.1–0.2 vol %) at the onset of melting where CO_2 is concentrated in the melt. That said, a critical requirement for a partial melt distribution to impact bulk conductivity is that the melt be well connected through the host rock. Evidence that partial melt in the mantle is well interconnected, even at low melt fractions, comes from laboratory simulations [e.g., *Toramaru and Fujii*, 1986; *Riley et al*., 1990; *Zhu et al*., 2011].

Carbonatite melts are at least two orders of magnitude more conductive than silicate melts [*Gaillard et al*., 2008; *Yoshino et al*., 2010]. Carbonatite melts can form in trace amounts deep in the mantle [*Dasgupta and Hirschmann*, 2006] and are thought to be stable in the upper asthenosphere beneath seafloor older than about 45 Ma [*Hirschmann*, 2010]. Because of their high conductivity, volume fractions as small as 0.01% have the potential to impact bulk conductivity at measurable levels, and carbonate melt is interconnected to fractions as low as 0.05 wt % [*Minarik and Watson*, 1995]. Silicate, carbonated silicate, carbonatite melts [*Hirschmann*, 2010; *Gaillard et al*., 2008], and hydrous silicate melts [*Ni et al*., 2011] could be stable in the LVZ depending on the pressure and temperature. Estimated melt fractions range from 0.05 to 0.1% if the melt is carbonatite [*Gaillard et al*., 2008; *Yoshino et al*., 2010, 2012], ~0.3% if carbonated silicate melt [*Hirschmann*, 2010], and 0.3–1% if hydrous silicate melt [*Ni et al*., 2011]. At higher melt fraction the melt interconnectivity increases, which in combination with the melt buoyancy can provide pathways for melt to migrate [*Karato*, 2012]. Yet at the very low melt fractions at which CO_2 bearing or carbonatite melts can impact bulk mantle conductivity, it has been argued that melt networks could be stable against upward buoyancy driven migration [*Sifre et al*., 2014], thereby removing one of the major arguments against widespread melt distributions in the upper asthenosphere.

2. Data

The MT component of the NoMelt experiment measured natural electric and magnetic field variations during a year-long deployment between 4 December 2011 and 7 January 2013. A linear array of six stations was deployed in a profile roughly parallel to the plate spreading direction (Table 1 and Figure 1), coincident with an array of ocean bottom seismographs. The region of study did not contain rugged or anomalous bathymetry such as seen at a mid-ocean ridge [*Baba et al*., 2006], nor any active volcanism, and therefore was expected to have a simple 2-D electrical structure (see Figure 1). Four out of six stations provided useful data with sufficient period range to constrain mantle structure at depths well beyond that predicted for the LAB in the studied region. Electromagnetic time series from each site were cleaned by removing obvious noise such as variations due to instrument settling or collection, data spikes, and steps in the field magnitude, and corrected for clock drift using magnetic field data from the INTErnational Real-time MAGnetic observatory NETwork (INTERMAGNET) Hawaiian station. These observatory data also served as a reference for instrument rotation, and as a remote reference for robust processing carried out with the bounded influence code, BIRRP [*Chave and Thomson*, 2003, 2004].

The final apparent resistivity and phase curves for all sites used during inversion are shown in Figure 2. Useful periods contained in the response function range from ~800 s out to 100,000 s, sufficiently long to probe through the upper mantle and down as far as the 410 km discontinuity. The calculated response functions from the four stations show dominantly 2-D characteristics, with significantly smaller diagonal elements relative to the off-diagonal elements in the impedance tensors (**Z**), regardless of the orientation of the tensor. The strong off-diagonal elements of the **Z** tensor describe the two modes of the 2-D MT response. Z_{xy} is the transverse electric (TE) mode corresponding to electric current flowing parallel to the regional electrical strike. Z_{yx} is the transverse magnetic (TM) mode, corresponding to the electric current flowing perpendicular to the electrical strike. The data were processed in a reference frame such that the *x* axis (the assumed electric strike) is perpendicular to the spreading direction. This particular rotation direction was chosen because the dominant seafloor fabric is aligned with the spreading ridge. Numerous seismic anisotropy studies using a variety of methodologies indicate that lithospheric fabric is aligned with fast wave speeds parallel to spreading direction [*Raitt et al*., 1969; *Nishimura and Forsyth*, 1989; *Montagner and Tanimoto*, 1991; *Wolfe and Solomon*, 1998; *Gaherty et al*., 2004]. The anisotropic inversion requires orthogonality between the primary conductivity axes. If conductivity is enhanced in the direction of plate-spreading, then this fabric would be orthogonal to our principal strike direction and would be identifiable by the inversion.

The NoMelt survey area was specifically chosen to be devoid of seamounts and large topographic features to ensure a limited amount of melt in the upper mantle. Variations in depth between each usable site was $<$60 m. Because the NoMelt region does not have significant bathymetric variation, which distorts the measured electric and magnetic fields, topographic corrections as described by *Baba and Chave* [2005] were not considered. A flat ocean floor was assumed and the shortest periods were masked prior to inverting which is where topographic effects are most significant [*Baba and Chave*, 2005; *Matsuno et al*., 2010].

Table 1. NoMelt MT Station Sites Used in Inversions and Corresponding Latitude, Longitude, Depth

Site	Latitude	Longitude	Depth (m)
M01	8°45′03.630″N	147°59′44.687″W	5179
M02	8°58′21.763″N	146°55′38.195″W	5226
M04	9°24′30.586″N	144°47′16.039″W	5167
M06	9°49′45.130″N	142°38′22.062″W	5181

The two modes show nearly identical phase trends and decreasing resistivity with increasing period, confirming the presence of a simple electrical structure and justifying our 2-D approach to inverting the responses.

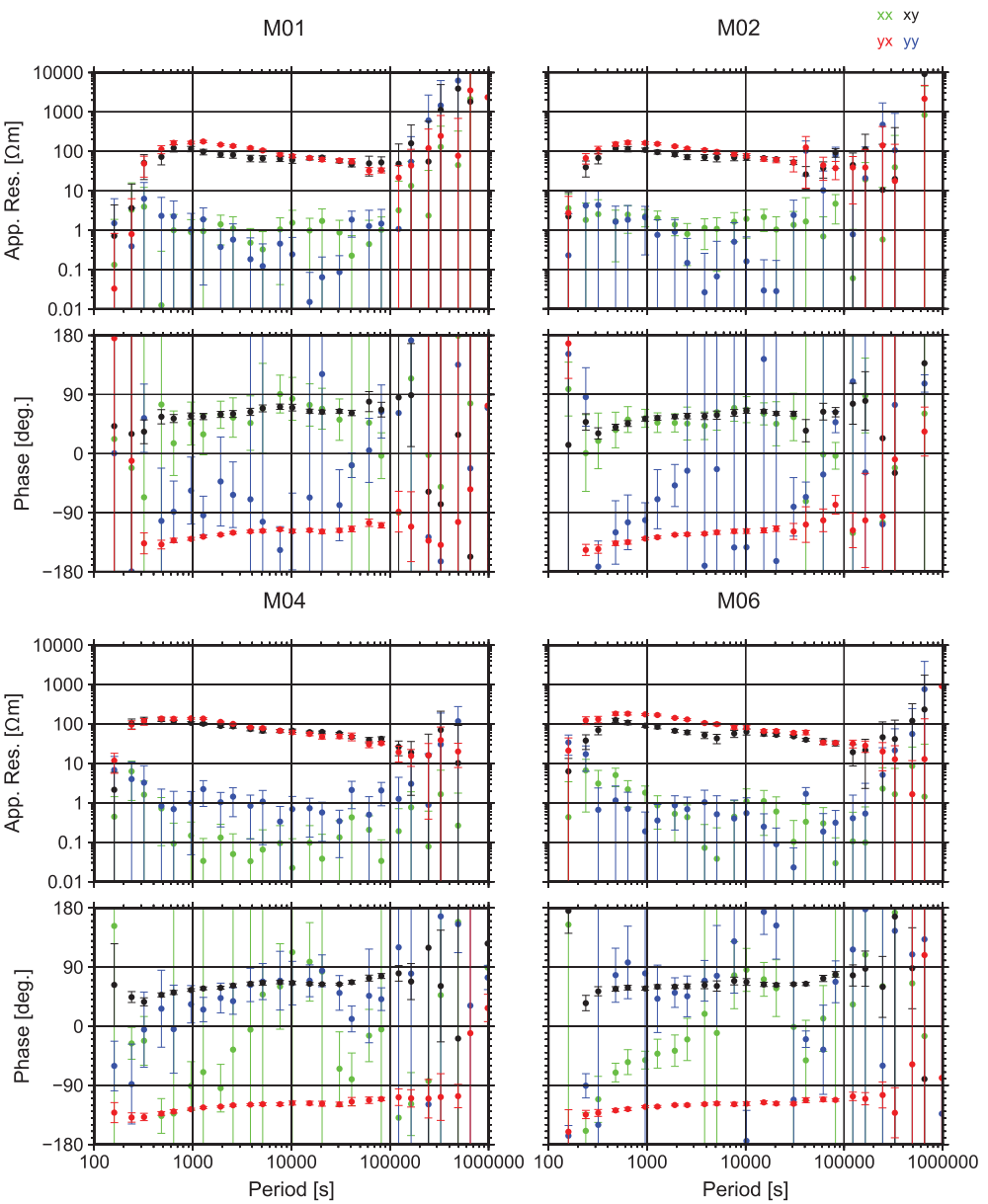

Figure 2. The apparent resistivity and phase curves versus data period from the four used stations is shown. The TE mode (Z_{xy}) and TM mode (Z_{yx}) are the black and red dots, respectively. The off-diagonal elements (green and blue dots) have low apparent resistivities and large errors suggesting that the NoMelt electrical structure is 2-D (see text).

3. Inversion Methods

MT resistivity and phase data were inverted for both isotropic and anisotropic electrical structure. Isotropic electrical models of the NoMelt mantle were derived using a 2-D regularized inversion scheme [*Rodi and Mackie*, 2001] implemented within the WinGLink software package. Previous MT investigations of the Pacific detected anisotropic conductivity distributions, in which the conductivity of the upper asthenosphere was greater in the (horizontal) direction of plate motion [*Evans et al*., 2005; *Baba et al*., 2006]. Anisotropy can lead to distorted structure if inverted using an isotropic code, therefore a 2-D anisotropic inversion scheme [*Baba et al*., 2006] was used to verify that the observed structure from isotropic inversions is accurate, or if electrically anisotropic features are present within the lithosphere-asthenosphere transition zone. The isotropic inversions result in a single resistivity model, whereas the anisotropic inversions solved for three separate models showing resistivity in the strike direction (ρ_{xx}) parallel to plate motion (ρ_{yy}) and in the vertical direction (ρ_{zz}). The anisotropic inversions of the NoMelt data resulted in the same structure as in the isotropic inversion and the difference between the horizontal directions ($\rho_{xx} - \rho_{yy}$) indicate that there is no significant electrical anisotropy required in the region to explain our data (Figure 3b). As a result, only the isotropic inversion is discussed for the remainder of this paper.

A variety of starting models and regularization parameters were used to explore model space during the inversion process. Starting models varied from uniform half-space models to layered models with structure introduced from assumed a priori knowledge or for hypothesis testing. In some cases the starting resistivity of the layers was simply varied, while in other cases the resistivity was locked, or a tear (relaxation of model smoothness) was placed at various depths to allow for sharper boundaries. Inversions with starting models containing tears were run to ensure that if a thin layer of high conductivity was present it was not being entirely smoothed out between the resistive lithosphere and conductive asthenosphere by the regularization scheme. Data error values were maintained at 10% for the apparent resistivity and 5% for the phase. Error floors on the apparent resistivity and phase of both modes were held at 5% during initial inversions. Generally, the two modes were inverted jointly because the two modes contain complementary information—the TE mode is most sensitive to continuous conductive structures in the strike (x) direction, and the TM mode is most sensitive to the regional structure and resistivity boundaries [e.g., *Wannamaker et al*., 1989]. Single-mode inversions were also completed and revealed that the TE mode was insensitive to the resistive lithosphere resulting in high conductivities at lithospheric depths. Therefore, in order to constrain lithospheric resistivities, later inversions had an increased error floor of 20% for the TE mode apparent resistivity. The smoothness regularization parameter, τ, was varied between 100 (smooth) and 0.01 (rough) to find the best fitting model that did not contain spurious structure. Models generated with large τ values (smooth models with poorer fits to the data) damped the uppermost lithospheric resistivity, potentially smoothing out important features. On the other hand, at small τ values (rough models with good data fit), the model became geologically implausible with oscillatory conductivity variations. Inversions were completed to investigate the data sensitivity to the lithospheric resistivity, the conductance of a possible high conductivity layer at the LAB, and the resistivity of the asthenosphere. Models were evaluated through RMS misfit values, smoothness, and geological plausibility. The RMS misfit of the preferred isotropic model at the various tau values ranged from 1.05 ($\tau = 0.01$) to 2.49 ($\tau = 100$), a small variation which further suggests that the NoMelt data are consistent with a moderately 2-D structure. Given that the resulting models showed very little lateral variability, the preferred isotropic 2-D conductivity model was averaged (in log domain) into a 1-D conductivity profile with depth (Figure 3c).

4. Results

The preferred 2-D isotropic conductivity model of the NoMelt region was derived from a layered starting model with a high resistivity lithosphere (10^4 Ωm) underlain by a 100 Ωm half-space. The inverted model contains a 2–30 Ωm conductive layer of variable thickness above the lithosphere. The electrical lithosphere extends to 80 km depth and high resistivities are maintained, although the final resistivity in the lithosphere was slightly reduced from the starting values (10^2–10^3 Ωm). Asthenospheric (>80 km depth) resistivities decreased to 25–75 Ωm (Figure 3a). After hundreds of iterations, the preferred model achieved an RMS misfit value of 1.21 (see Figure 4). The same general structure was achieved throughout all inversions, regardless of starting model.

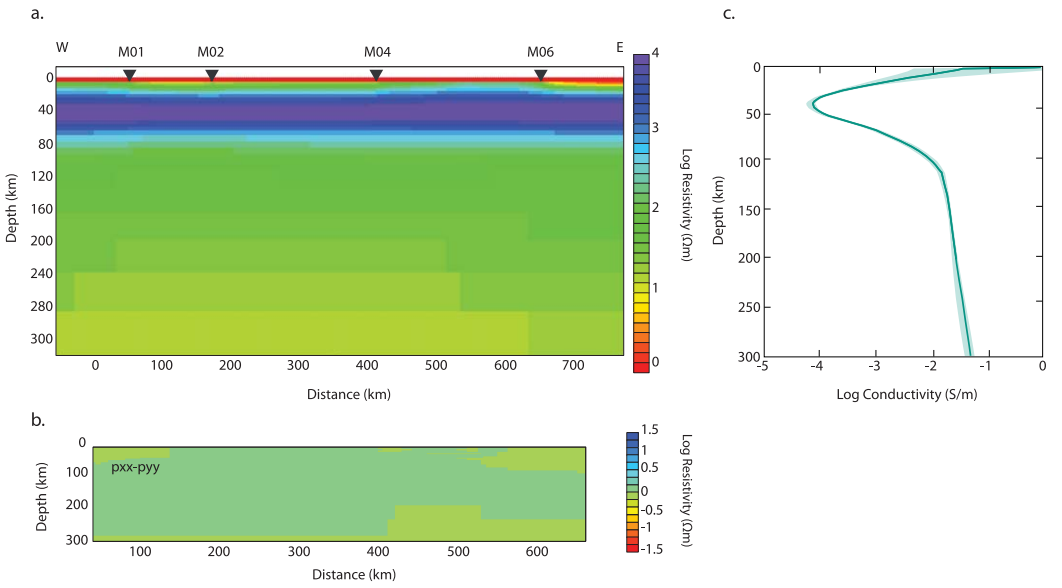

Figure 3. (a) Our preferred 2-D isotropic resistivity model for the NoMelt region. (b) The difference between resistivity in the horizontal directions ($\rho_{xx} - \rho_{yy}$) of the 2-D anisotropy model. The log resistivity values indicate that there is no significant electrical anisotropy required in the region to explain our data. (c) The corresponding 1-D model produced from averaging the 2-D model resistivities with depth (bold teal line) and the maximum and minimum resistivity values with depth (shaded range).

In all cases, the resistivity within the cool lithosphere is not as high as might be expected, but this is a resolution issue inherent to the MT technique. Inversions of synthetic data generated from a model with a highly resistive lithosphere overlying a range of lower-lithosphere and asthenospheric structures show that the resistivity within the lithosphere is always reduced as a result of the combined effects of a lack of sensitivity and regularization, with no loss of fit between the model and the data [*Evans et al.*, 2011].

No models were obtained from our field data that contained a layer of low ($<$10 Ωm) resistivity in the upper electrical asthenosphere or within the LAB region, and the inversion algorithm removed any such layer when imposed in starting models. Synthetic tests suggest that MT data can have sensitivity to such a feature. When a melt layer was forced under the resistive lithosphere, the model RMS misfit increased to values greater than 5 and resulted in a poorer fit to the data (see Figure 4). Starting models that contained tears resulted in oscillatory structure that lead to a highly resistive asthenosphere, suggesting that the relaxation of regularization in this case was equivalent to lowering the τ value and the data were likely overfit in these examples.

The 1-D conductivity profile of the NoMelt model captures the characteristics of the 2-D structure and shows a smooth transition from a resistive lithosphere to an increasingly conductive asthenosphere (Figure 3c). This lack of a conductive layer in the LAB transition zone is in contrast to profiles from the MELT area [*Evans et al.*, 2005], SERPENT experiment [*Naif et al.*, 2013], and the Philippine Sea [*Baba et al.*, 2010] (see Figure 5). Observations at the Southern East Pacific Rise highlight an electrically conductive and anisotropic layer in the asthenosphere beneath a resistive (anhydrous) upper plate [*Evans et al.*, 2005; *Baba et al.*, 2006]. The conductivity of the asthenosphere in the MELT region can be explained by a damp composition, but could also be explained by a small amount of partial melt. In contrast, an anisotropic conductor seen off Nicaragua [*Naif et al.*, 2013] is sufficiently conductive to require the presence of melt in the upper electrical asthenosphere, although for melting to occur the mantle must also be damp. One further observation, which is supportive of a damp and possibly melt bearing upper asthenosphere comes from ~30 Ma lithosphere in the Philippine Sea [*Baba et al.*, 2010] where a conductive upper asthenosphere is consistent with a small silicate melt fraction. Thus, to date, we have three observations of an electrically conductive layer in the upper mantle in relatively young oceanic lithosphere that are each consistent with the presence of melt and H_2O (dissolved hydrogen) at asthenospheric depths to aid with the interpretation of the NoMelt data.

The next section discusses the possible thermal, dissolved H_2O, and partial melt contributions to the observed conductivity structure in the NoMelt region and clarifies which mechanism is most likely

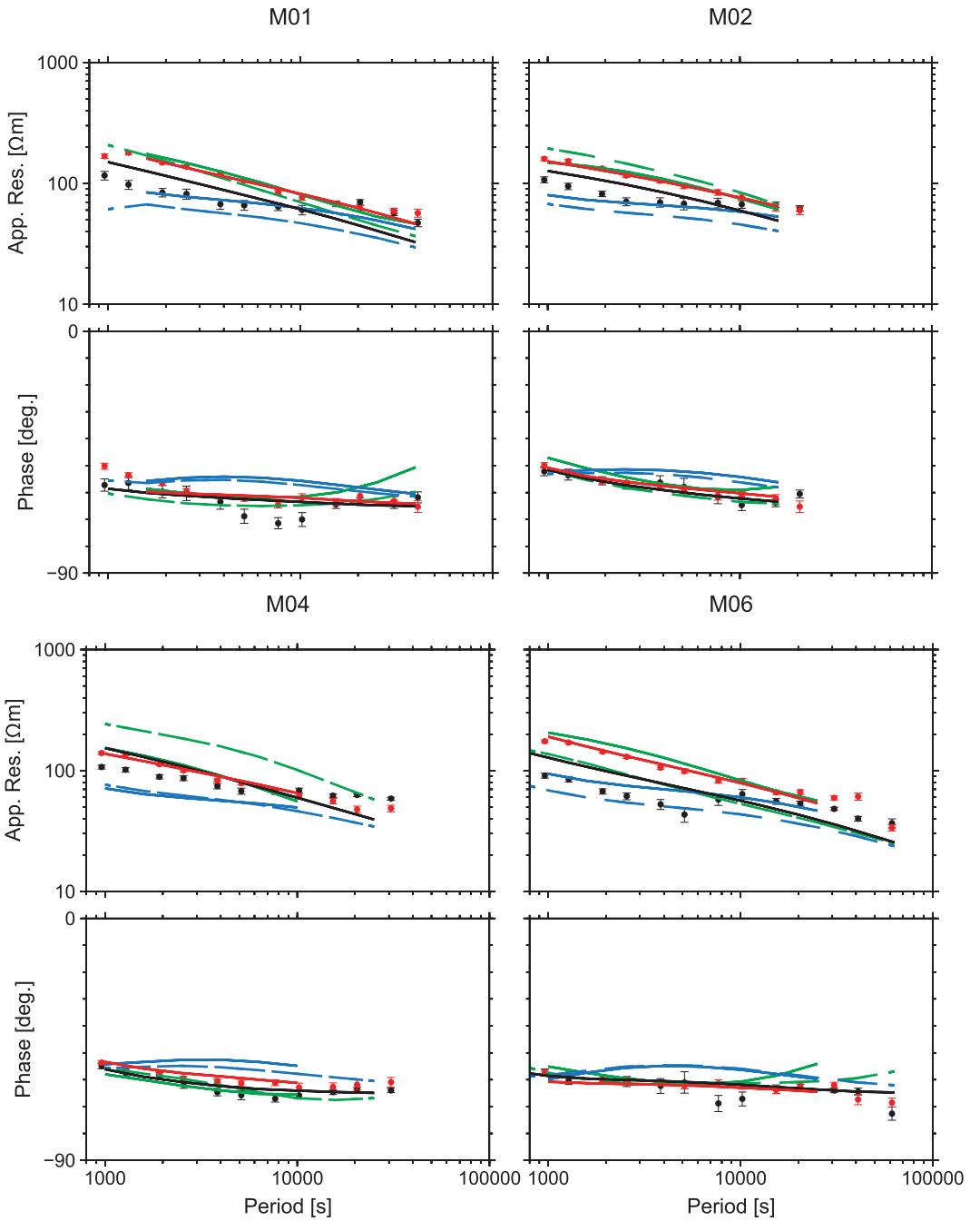

Figure 4. Inversion model responses for the preferred isotropic 2-D model (TM mode in bold red line; TE mode in bold black line), an isotropic 2-D model with a forced 15 Ωm melt layer at the base of the lithosphere (blue lines; TM mode solid, TE mode dashed), and an isotropic 2-D model with a 0.3°C/km thermal gradient within the asthenosphere (green lines; TM mode solid, TE mode dashed). See section 4 for discussion.

responsible for the weakening of the asthenosphere based on our MT observations. The comparison of the NoMelt profile with profiles from other surveys (Figure 5) seems to suggest that dissolved H_2O and partial melt mechanisms are not as influential in the NoMelt region as in other regions.

5. Discussion

The observed conductivity in the NoMelt region shows a simple upper mantle electrical structure under the 70 Ma Pacific plate. The 1-D profile generated allows for a quick conversion of the model into temperature,

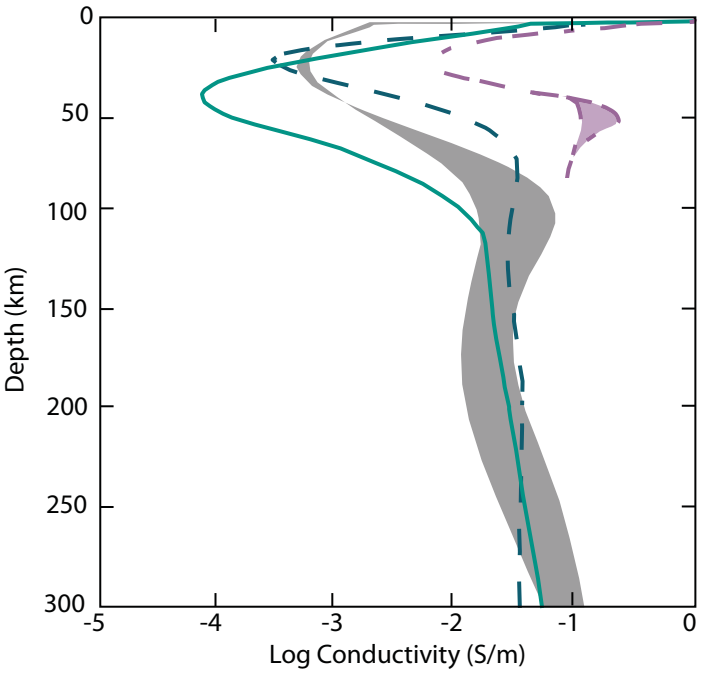

Figure 5. 1-D log conductivity versus depth profile of the averaged NoMelt 2-D model (teal) compared to MT models from other seafloor areas is shown. In general, the NoMelt LAB is less conductive than the MELT (gray region), SERPENT (purple dashed region), and Philippine Sea (teal dashed) LAB. The MELT and SERPENT regions indicate the amount of electrical anisotropy observed.

dissolved H_2O, and interconnected partial melt—three major mechanisms influencing mantle conductivity. As these components have strong interdependency and influence the observed conductivity in a complex manner, we chose to interpret the model in a sequential manner starting with the simplest, first order control, a direct conversion of conductivity to temperature, then examine potential effects of added dissolved H_2O, and finally for an additional interconnected partial melt component.

5.1. Thermal Contribution

We first converted the conductivity profile directly to a temperature profile between 50 and 300 km depth (Table 2 and Figure 6), using the SEO3 at quartz-magnetite-fayalite buffer (QFM) model for anhydrous olivine conductivity [*Constable*, 2006]. Previous studies [e.g., *Evans et al*., 2005] have used the SO2 model [*Constable et al*., 1992] for the background anhydrous olivine conductivity. SO2 is appreciably less conductive than SEO3 (QFM), and a similar direct conversion to temperature using SO2 would predict temperatures that are hotter by roughly 200°C at 200 km depth, which seems unreasonably hot. Similarly, if the anhydrous olivine conductivity is calculated using SEO3 at a more reducing buffer such as iron-wustite (IW), predicted temperatures would also be hotter, but in this case only by about 60°C at 200 km. Thus, there is some variability in the estimation of temperature within the asthenosphere based on the choice of oxygen fugacity and the dry olivine conductivity model.

The thermal adiabatic gradient of our temperature profile calculated from SEO3 (QFM) was determined by calculating the slope of the temperature profile well within the convecting asthenosphere between depths of 150 and 300 km. The resulting adiabat has a thermal gradient of 0.5°C/km and a potential temperature of 1374°C. Deviation of our temperature profile from the calculated adiabat suggests upper limits on plate thickness and basal temperature in the NoMelt region of 110 km and 1424°C, respectively. These values are within the realm of likely mantle temperatures, but it is not clear if they are consistent with other constraints on mantle structure. Following *Crosby et al*. [2006], we define the base of the lithospheric plate by the intersection of the conductive plate geotherm with the mantle adiabat. To obtain this estimate and provide a better constraint on plate thickness, we calculated the conductive plate geotherm of the NoMelt mantle from the temperatures within the resistive lithosphere of the 2-D electrical model at depths between 50 and 80 km. This resulted in a plate geotherm that intersected the adiabat at a depth of 91 km with a corresponding basal temperature of 1415°C (see Figure 6).

Depth-age relationships of oceanic plates are useful in determining asymptotic plate thicknesses [*Parsons and Sclater*, 1977; *Stein and Stein*, 1992; *Crosby et al*., 2006], and with a carefully chosen data set, can help verify our calculated mantle plate thickness and basal temperature. Previous plate cooling studies have determined that the asymptotic Pacific plate thickness is between 90 and 125 km [*Parsons and Sclater*, 1977; *McKenzie and Bickle*, 1988; *Stein and Stein*, 1992; *Crosby et al*., 2006]. Our next step, therefore, was to investigate the depth-age relationship following the procedure of *Crosby et al*. [2006] for the segment of the Pacific plate between the Clarion and Clipperton fracture zones from 70 Ma to the East Pacific Rise to determine if our plate model derived from an unconstrained conversion of our NoMelt model was

Table 2. Thermal, H_2O, and Melt Model Results With Depth

Depth	Temperature of Plate Model With 0.5°C/km Gradient (°C)	Temperature of Plate Model With 0.3°C/km Gradient (°C)	Bulk Mantle Water Content From DK Model (ppm)[a]	Bulk Mantle Water Content From UHO Model (ppm)[a]	Melt Content Assuming DK Water Content + 100 ppm CO_2 (vol %)	Melt Content Assuming UHO Water Content + 100 ppm CO_2 (vol %)
50	902	902	4 (1)	13 (3)	0.069	0.069
60	1053	1053	0 (0)	0 (0)	0.073	0.073
70	1196	1196	0 (0)	0 (0)	0.075	0.075
80	1306	1306	0 (0)	0 (0)	0.075	0.075
90	1360	1360	0 (0)	0 (0)	0.0096	0.0096
100	1400	1400	0 (0)	16 (4)	0.065	0.015
110	1424	1419	0 (0)	61 (17)	0.060	0.019
120	1429	1422	0 (0)	84 (24)	0.058	0.058
130	1434	1425	3 (1)	103 (30)	0.056	0.056
140	1439	1428	3 (1)	118 (35)	0.054	0.024
150	1444	1431	3 (1)	129 (39)	0.052	0.053
160	1449	1434	7 (2)	141 (43)	0.052	0.028
170	1454	1437	6 (2)	150 (46)	0.028	0.029
180	1459	1440	6 (2)	159 (49)	0.048	0.048
190	1464	1443	6 (2)	172 (53)	0.045	0.045
200	1469	1446	6 (2)	185 (57)	0.039	0.040
210	1474	1449	10 (3)	199 (61)	0.039	0.040
220	1479	1452	10 (3)	216 (66)	0.039	0.040
230	1484	1455	10 (3)	234 (71)	0.039	0.040
240	1489	1458	13 (4)	254 (77)	0.039	0.040
250	1494	1461	13 (4)	276 (83)	0.039	0.040
260	1499	1464	17 (5)	297 (89)	0.039	0.040
270	1504	1467	17 (5)	321 (96)	0.039	0.040
280	1509	1470	20 (6)	345 (103)	0.039	0.040
290	1514	1473	23 (7)	368 (110)	0.040	1.00
300	1519	1476	23 (7)	394 (118)	0.040	1.00

[a]Corresponding olivine water contents are listed in parentheses.

consistent with the seafloor subsidence. Seafloor older than about 80 Ma shows anomalous bathymetry and was not considered in our analysis [*Crosby et al.*, 2006]. The segment bathymetry is consistent with a suite of possible basal temperature-asymptotic plate thickness pairs ranging from a hot, thin plate with a basal temperature of 1500°C and a plate thickness of 75 km, to a colder, thicker plate with a basal temperature of 1250°C and a 125 km thick plate. The plate thickness and basal temperature that best predict bathymetric variations, and which generate a thermal profile most consistent with our observations from our 2-D inverse model, are 86 km and 1412°C, respectively. This result is very close to the plate thickness and basal temperature that we predicted by only considering the converted temperature profile.

From these analyses, we derive a plate cooling mantle geotherm that results in a conductivity-depth profile that matches the observed NoMelt profile except in the lowermost lithosphere where the geotherm predicts slightly more resistive structure (Table 2 and Figure 6). However, while a mantle thermal gradient of 0.5°C/km is consistent with the range of estimated adiabatic gradients [*Katsura et al.*, 2010, and references therein; *Stixrude and Lithgow-Bertelloni*, 2005], other estimates suggest a lower mantle gradient of 0.3°C/km [e.g., *Turcotte and Schubert*, 2002]. Therefore, we also constructed a background thermal model from the plate geotherm derived from bathymetry, but with a mantle adiabatic gradient of 0.3°C/km. This lower gradient background thermal model has the same plate thickness and basal temperature as the previous model, but a slightly higher potential temperature of 1386°C and a conductivity depth profile that is slightly more resistive than the observed NoMelt profile in both the lower lithosphere and asthenosphere (Table 2 and Figure 6). Forward modeling of our preferred electrical model with a 0.3°C/km thermal gradient showed a poorer fit to the data (see Figure 4), which indicates that our data are sensitive to the adiabatic thermal gradient. As a result, conductivities at depths below 50 km are under-predicted by the 0.3°C/km mantle gradient thermal model and an additional solid state or melt mechanism is needed to explain the observed conductivity profile.

5.2. Dissolved H_2O Contribution

The first mechanism we considered to enhance the background thermal conductivity profile to match our observed profile was the solid state contribution of dissolved H_2O in mantle minerals. Current knowledge of

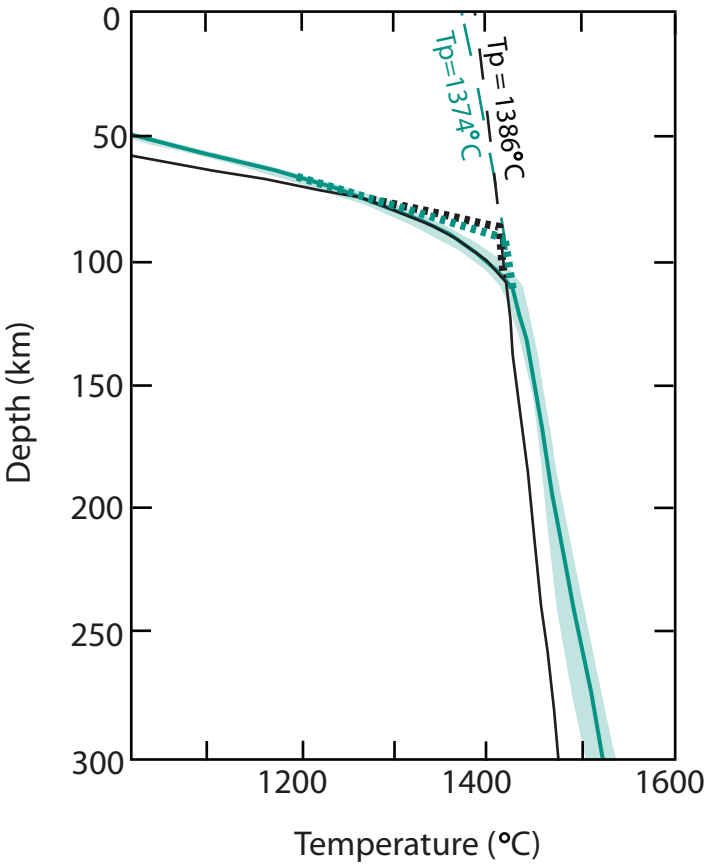

Figure 6. Shown is the direct temperature conversion of the observed NoMelt conductivity with depth (teal). The shaded region shows the maximum and minimum temperature converted from conductivity. This thermal profile was calculated to have an adiabatic thermal gradient of 0.5°C/km, a potential temperature of 1374°C (dashed teal line), and a plate thickness of 91 km (dotted teal line). Also shown is the background plate cooling thermal model (black) with an adiabatic thermal gradient of 0.3°C/km, a potential temperature of 1386°C (dashed black line), and a plate thickness of 86 km (dotted black line). The plate thickness and basal temperature from the background thermal model is determined by bathymetric variations (see section 5.1 for discussion).

mantle mineral conductivity with dissolved hydrogen is focused on olivine—the major phase (60%) in the upper mantle—due to a lack of compelling data on the conductivity of other nominally anhydrous phases, such as pyroxenes, for upper mantle conditions [*Dai and Karato*, 2009]. Such focus limits most MT studies to assume that hydrous olivine is the dominant conducting phase when considering a subsolidus mechanism. Thus, we used two of the most recent models for how dissolved H_2O in olivine enhances the measured conductivity: the UHO model [*Gardes et al*., 2014] and a model that includes high-temperature conductivity measurements made at temperatures appropriate for the asthenosphere from *Dai and Karato* [2014] (referred to as the DK model).

The UHO model reanalyzes previously published conductivity measurements to form a single Arrhenius relationship that satisfies all the data. The relationship involves anhydrous and hydrous conductivity mechanisms that relate the conductivity of olivine to its H_2O content such that

$$\sigma_{UHO} = \sigma_0^V \exp\left(-\Delta H^V/RT\right) + \sigma_0^P \exp\left(-\Delta H^P/RT\right) + \sigma_0^H C_{H_2O} \exp\left[\left(-\Delta H^H - \alpha C_{H_2O}^{1/3}\right)/RT\right] \quad (1)$$

where σ_{UHO} is the conductivity of hydrous olivine, σ_0^V, σ_0^P , and σ_0^H are the preexponential factors for the anhydrous vacancy and polaron terms, and the hydrous conductive process, respectively, ΔH^V, ΔH^P, and ΔH^H are the corresponding activation enthalpies, R is the gas constant, T is the absolute temperature, and C_{H_2O} is the concentration of H_2O dissolved in olivine. The DK model produces a similar relationship to that found for previous conductivity measurements but adds new measurements made at higher temperatures that capture a distinct high-temperature conduction mechanism in olivine. The resulting conductivity equation is

$$\sigma_{DK} = C_w\left[\sigma_0^1 \exp(-\Delta H^1/RT) + \sigma_0^2 \exp(-\Delta H^2/RT)\right] + \sigma_{SEO3} \quad (2)$$

where σ_{DK} is the hydrous olivine conductivity, σ_0^1 and σ_0^2 are fitted preexponential terms, and ΔH^1 and ΔH^2 are the corresponding activation enthalpies. The σ_{SEO3} term accounts for a parallel anhydrous conductivity that is needed to fully describe the mantle conductivity and which is important when conductivities suggest small mantle H_2O contents. *Dai and Karato* [2014] developed a separate relationship for each olivine axis (a, b, and c) from which we calculated the geometric mean in order to get a relationship applicable to a bulk isotropic mantle as observed in the NoMelt region.

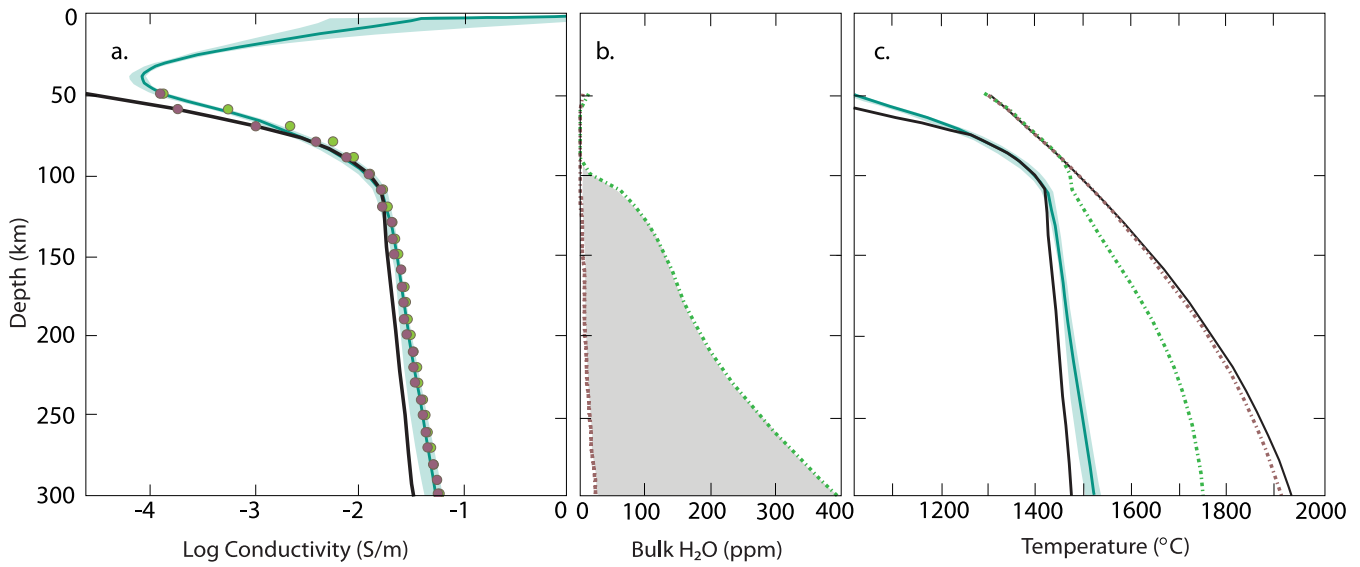

Figure 7. (a) Shown is the observed NoMelt conductivity profile with depth (teal). The teal region indicates the maximum and minimum conductivity from the 2-D model (as in Figure 3). The conductivity calculated from the background thermal model (black), and the calculated conductivities of the two hydrated olivine models with depth in 10 km intervals (DK: purple dots; UHO: green dots). The plot shows how H_2O increases the conductivity from the background thermal profile (black) to our observed profile (teal). (b) The range of H_2O estimates from both hydrous olivine models with depth for the NoMelt mantle (DK: purple dashed line; UHO: green dashed line; also see Table 2). The shaded region shows the possible bulk mantle H_2O. (c) Shown are the thermal profiles as in Figure 6. Also shown are the nominally anhydrous solidus (solid thin black line) and the partially hydrated solidi calculated from the two hydration models (DK: purple dashed; UHO: green dashed). From the plot, it is clear that our observed profile does not cross any solidus. Therefore, for melt to be stable in the NoMelt mantle, CO_2 would have to decrease the solidus temperature further than the partially hydrated solidi (see section 5.3 for explanation).

Using these two hydrous olivine models and our background thermal model, we varied olivine H_2O content from 0 to 1000 ppm in 1 ppm intervals then compared the calculated hydrous conductivity profiles to our observed conductivity model for the NoMelt region. By minimizing the difference between our observed profile and the hydrous conductivity profiles, we estimate the H_2O content of olivine starting in the lower lithosphere at 50 km down to 300 km depth in 10 km intervals (Table 2 and Figure 7a). Both models predict variable olivine H_2O contents with depth, but both models agree that while our background thermal model is slightly more resistive than the observed profile in the lithosphere (<80 km) there should be little to no H_2O in this region otherwise the hydrated olivine conductivity is more conductive than the NoMelt profile. Outside of the lithosphere, the two models predict different H_2O contents with DK predicting between only trace amounts between 0 and 7 ppm and UHO predicting between 0 and 118 ppm.

While many MT studies go on to discuss whether the calculated H_2O content of the olivine grains is consistent with the predicted oceanic upper mantle bulk H_2O contents of 50–200 ppm [*Michael*, 1988; *Saal et al*., 2002; *Simons et al*., 2002; *Workman and Hart*, 2005], most fail to consider the corresponding H_2O content of the other upper mantle minerals (orthopyroxene, clinopyroxene, and spinel or garnet). While these minerals may not greatly influence the measured conductivity, they do impact the total dissolved H_2O in the mantle. In order to determine the corresponding bulk mantle H_2O contents from the calculated olivine H_2O contents, we conducted a mass balance calculation dependent on the mineral modal proportions and mineral/mineral partition coefficients for H_2O.

The mineral modal proportions (Φ^{min}) and the partition coefficients for H_2O between opx and melt ($D_H^{opx/melt}$), olivine and melt ($D_H^{ol/melt}$), spinel and melt ($D_H^{sp/melt}$), and garnet and melt ($D_H^{gt/melt}$) are based on the work by *Hirschmann et al*. [2009] who determined the partition coefficients for olivine, spinel, and garnet and melt in the upper mantle to be 0.0017, 0, and 0.003, respectively. The partition coefficient for opx is dependent on the Al content of the pyroxene. Pyroxene composition changes with pressure such that increasing pressure increases the Al content until the garnet stability field where Al goes into the garnet phase. Using the relationships described in *Hirschmann et al*. [2009] our $D_H^{opx/melt}$ ranges from 0.01 to 0.02 where $D_H^{opx/melt}$ increases with depth until spinel-to-garnet transition is reached. The partition coefficient of H_2O between cpx and melt was taken from the work of *O'Leary et al*. [2010] which considers the effect of

varying cpx composition along a mantle adiabat, particularly tetrahedral Al ($^{IV}Al^{3+}$), on H_2O partitioning. The majority of H^+ within the cpx structure is incorporated through a coupled substitution with $^{IV}Al^{3+}$ that is sensitive to the phase composition, but not to pressure and temperature. At pressures less than 5–7 GPa, the Al content of cpx is similar to that of opx, thus we were able to use the same relations described in *Hirschmann et al*. [2009] to calculate the Al content of cpx. From this Al content, we were able to prescribe a conservative (upper) estimate of 0.02 for $D_H^{cpx/melt}$ based on *O'Leary et al*. [2010] (their Figure 6 and equation (11)).

We then calculated the bulk mantle H_2O content from the inferred olivine H_2O content and partition coefficients using the following equation:

$$Bulk\ Mantle\ H_2O = \Phi^{ol}\ C_w + \Phi^{opx}\ C_w\ D_H^{opx/melt}/D_H^{ol/melt} + \Phi^{cpx}\ C_w\ D_H^{cpx/melt}/D_H^{ol/melt} + \Phi^{gt}\ C_w\ D_H^{gt/melt}/D_H^{ol/melt} \quad (3)$$

where the garnet (gt) contribution is added at pressures greater than 2.8 GPa. Based on thermodynamic considerations, the olivine-melt and garnet-melt partition coefficients should also be dependent on pressure, but current experimental data do not capture significant changes at pressures below 5–7 GPa [*Hirschmann et al*., 2009]. Our considered depths reach pressures up to 10 GPa, therefore the determined partition coefficients represent minimums.

The resulting bulk mantle H_2O content estimated from both hydrous olivine models over the depth range investigated are listed in Table 2 and shown in Figure 7b. The lower lithosphere requires some H_2O to enhance the conductivity from that of anhydrous olivine to the observed profile. The accuracy of this H_2O estimate is uncertain because of uncertainties in $D_H^{min/melt}$ values, phase compositions, phase proportions [see *Hirschmann et al*., 2009], and because the regularization used during inversion generates smooth models with gradual conductivity variations rather than sharp boundaries. This smoothing could bring the conductivity of the lower lithosphere to higher values than reality due to the influence of the conductive asthenosphere immediately below.

As expected the UHO model predicts much higher olivine and bulk mantle H_2O contents (see Figure 7b). This difference is due to two major differences between the DK and UHO conductivity models. First, each model has different conduction mechanisms operative at high temperature, with the DK model requiring significantly lower H_2O contents to achieve higher conductivities. This high-temperature conduction mechanism has been previously hypothesized [*Karato*, 2013], but never before measured due to the difficulty in conducting high-temperature experiments with constant H_2O contents. Second, our DK hydrated olivine conductivity model includes the same anhydrous term used to derive our background thermal model whereas the UHO model uses different anhydrous terms based on a data set that is somewhat less conductive than SEO3 (QFM) and asthenospheric temperatures [*Xu et al*., 2000]. The less conductive UHO anhydrous terms result in higher estimates of H_2O contents in order to match the observed NoMelt conductivity. The SEO3 (QFM) model is considerably more conductive than other published models of anhydrous olivine conductivity [*Constable et al*., 1992; *Xu et al*., 2000] and the reasons behind this are discussed in the original article [*Constable*, 2006]. If instead of the SEO3 (QFM) model we used the SO2 anhydrous olivine model [*Constable et al*., 1992] to calculate our anhydrous thermal conductivity and DK H_2O content, then either temperatures are ~200°C hotter or, for the thermal profile on a 0.3°C/km adiabat used above, the conductivity of the geotherm drops by almost a full order of magnitude in the asthenosphere. While this change does not impact the H_2O contents predicted by the UHO model, it drastically changes the H_2O contents predicted by the DK model to unreasonably large amounts such that the entire NoMelt thermal profile lies above the H_2O-undersaturated solidus and pervasive melting must occur—a feature not seen in the NoMelt data. On the other hand, the SEO3 (IW) model either requires that the mantle temperatures are ~60°C hotter, or the conductivity of the geotherm on a 0.3°C/km adiabat drops by half an order of magnitude. In this case, the predicted bulk mantle H_2O contents from the DK model increase from the predictions of SEO3 (QFM) by 20 ppm at 300 km depth, which is insufficient to lower the H_2O-undersaturated solidus to the point where it crosses the NoMelt thermal profile. Therefore, we conclude that, since the SEO3 (QFM) model resulted in the lowest H_2O contents from the DK model and the UHO model (with separate anhydrous terms) predicted the highest H_2O contents, these options provide the most conservative estimates of the olivine and bulk mantle H_2O content.

Petrologic constraints suggest that the source mantle H_2O content for oceanic basalts is between 50 and 200 ppm [*Michael*, 1988; *Saal et al*., 2002; *Simons et al*., 2002; *Workman and Hart*, 2005]. In addition, experimental storage capacity data suggest that upper mantle peridotite can hold up to ~700 ppm at 8 GPa [*Ardia et al*., 2012], though CO_2 may decrease this capacity by a factor of 2 [*Yang et al*., 2014]. Estimated bulk H_2O contents from the DK model remain below these constraints throughout the mantle based on the SEO3 (QFM) anhydrous model, while the UHO model predicts H_2O contents within the independently constrained ranges until a depth of 210 km, where H_2O contents reach over 200 ppm and rise to almost 400 ppm by 300 km. The peridotite storage capacity may very well be exceeded by 300 km dependent on the partitioning of H_2O between garnet and olivine [*Ardia et al*., 2012], which would suggest that melt or a fluid could be stable at greater depths and higher temperatures. In order to investigate whether our observed conductivities are below the estimated partially hydrated solidus, our next step was to calculate the solidi corresponding to both the UHO and DK estimated mantle H_2O contents to compare to the NoMelt thermal profile.

We modeled the anhydrous peridotite solidus using the parameterization from *Hirschmann* [2000].We then calculated the peridotite partition coefficient $D_H^{perid/melt}$ based on the mineral abundances and $D_H^{min/melt}$ values previously described. $D_H^{perid/melt}$ increases from 0.007 to 0.009 until the onset of garnet stability when the opx abundance and pyroxene aluminum content decreases. At higher pressures, the $D_H^{perid/melt}$ decreases to 0.005. These values match the values determined by *Hirschmann et al*. [2009] who verified the peridotite partition coefficient values through a Monte Carlo simulation to minimize the influence of the uncertainties in $D_H^{min/melt}$, and mineral abundances. The $D_H^{perid/melt}$ values were then used to calculate the fraction of H_2O in the melt phase at the solidus based on the parameterization of *Katz et al*. [2003] where the decrease in solidus temperature is proportional to the dissolved bulk H_2O content from each model.

At no point does our preferred NoMelt thermal profile cross either H_2O-undersaturated peridotite solidus (Figure 7c). Taken at face value, this suggests that melting is unlikely at any depth in the NoMelt asthenosphere and that H_2O dissolved in olivine is solely responsible for the observed conductivity.

5.3. Melt Contribution

While the combination of a hydrous mantle and a plate cooling model with a low adiabatic thermal gradient offer a self-consistent, solid-state explanation for the observed mantle conductivity in the NoMelt region, the presence of CO_2 may provide a means to induce melting even at low temperatures, so we place constraints on how much melt could be consistent with our observed profile. Recent melt fraction estimates in the asthenosphere from MT studies range from 0.5 to ~2 vol % dependent on whether silicate, hydrous silicate, or carbonatite melt compositions are considered [*Naif et al*., 2013; *Baba et al*., 2010]. These melt fractions were estimated by using observed conductivity profiles and simultaneously assuming a background conductivity and a melt conductivity at a certain pressure, temperature, and H_2O content, but we have found that our predicted H_2O contents should not be enough to lower the solidus for melting.

Recent laboratory work has shown that CO_2 drastically influences the melt conductivity at the initial stages of melting [*Sifre et al*., 2014], and stabilizes carbonated silicate melt in the upper asthenosphere [*Hirschmann*, 2010]. The oceanic mantle is thought to contain 25–100 ppm CO_2 [*Hirschmann and Dasgupta*, 2009], but some estimates range to hundreds of ppm [e.g., *Sifre et al*., 2014]. Mantle CO_2 content will vary with degree of melting and oxidation [*Dasgupta et al*., 2013], as well as the stability of a CO_2 phase. For this study, we assume that the combination of the H_2O contents calculated previously and a certain defined bulk CO_2 is sufficient to lower the H_2O-undersaturated peridotite solidus temperature so that some melt is stable in the NoMelt mantle (see Figure 7c). We assumed what we believe to be a conservative bulk mantle CO_2 content of 100 ppm based on the above predictions.

Melt conductivity depends strongly on the CO_2 content of the melt, which depends strongly on melt fraction, since CO_2 is essentially perfectly incompatible in the solid [*Sifre et al*., 2014]. This behavior means that the melt conductivity, melt CO_2 content, and melt fraction are all unknown parameters that vary as melting progresses, and they cannot be simultaneously determined using MT data alone. In order to solve for the possible melt fractions in the NoMelt asthenosphere, we assumed the same volatile mantle partitioning as *Sifre et al*. [2014] and determined the melt conductivity at a range of melt fractions. Although there is no strong evidence for a highly conductive layer within the LAB region of the NoMelt profile, we chose to vary

melt fractions between 0 and 5 vol %—a larger range than *Utada and Baba's* [2014] determination for old oceanic mantle (100 Ma).

The background mantle conductivity was determined by the amount of H_2O that remains in the residual peridotite based on H_2O partitioning. Combined with the corresponding carbonated silicate melt conductivity, we were able to calculate the bulk peridotite conductivity at each melt fraction considered from the Hashin-Shtrikman (HS) upper bound mixing law [*Hashin and Shtrikman*, 1962]. The resulting bulk conductivities were directly compared to the observed NoMelt profile, and the best fitting melt fractions at each depth in the asthenosphere were chosen by minimizing the difference between the observed and calculated bulk conductivities.

Regardless of whether UHO or DK bulk H_2O contents are used for the calculation of melt conductivities, melt fractions required to explain the observed NoMelt electrical conductivity remain at or below 1 vol % (Table 2). The DK model predicts a maximum melt fraction of 0.075 vol % at 80km showing the potential for a small amount of carbonated hydrous silicate melt at our observed electrical LAB depth. On the other hand, the UHO model predicts a maximum melt fraction of 1.0 vol % at 300 km, but again predicts only a melt fraction of 0.075 vol % at the electrical LAB. Therefore, if a mantle CO_2 content of 100 ppm is accurate and is able to decrease the solidus enough for melting to occur, only trace amounts of melt would be present at the NoMelt electrical LAB. The lack of significant melt at the depths corresponding to the LAB further supports a hydrous mechanism explanation for the observed conductivity.

5.4. Anisotropy

In contrast to two recent oceanic studies [*Evans et al*., 2005; *Naif et al*., 2013], our data do not require electrical anisotropy. Furthermore, a possible interpretation of the MT model for the NoMelt upper mantle uses dissolved H_2O to explain slightly elevated conductivities. Initial interpretations of the southern portion of the MELT experiment also invoked dissolved H_2O to explain the observed conductivity, but these studies suggested higher H_2O contents than for the NoMelt region [*Evans et al*., 2005; *Baba et al*., 2006]. Anisotropy in the MELT area showed that conductivities differed by about a factor of 4–5 between the plate spreading and strike directions (see Figure 5). This result is consistent with predictions of conductivity based on diffusion of hydrogen, which is significantly faster along the olivine *a* axis [*Kohlstedt and Mackwell*, 1998]. Although subsequent published conductivity measurements are less conclusive on whether hydrous olivine conductivity is anisotropic [*Yoshino et al*., 2006; *Poe et al*., 2010], recent data do show evidence for higher conductivity along the *a* axis [*Dai and Karato*, 2014], with a factor of 2–3 possible for a mantle aggregate. While dissolved H_2O may be influencing the NoMelt mantle conductivity, we do not observe any electrical anisotropy. The most likely explanation is that the H_2O contents are sufficiently low as to not induce detectable electrical anisotropy in an imperfectly aligned mantle fabric [e.g., *Yang*, 2012].

6. Conclusions

The NoMelt experiment set out to image the structure of the central Pacific plate lithosphere and the LAB transition. Electrical conductivity is sensitive to temperature, dissolved H_2O, and interconnected melt giving electromagnetic data the ability to help determine the mechanisms responsible for the rheological transition from the rigid lithosphere to the weak asthenosphere. Results from 2-D isotropic and anisotropic inversions of MT data indicate that the electrical structure of the NoMelt region is isotropic and does not contain a highly conductive layer under the resistive electrical lithosphere. Therefore, based on first order interpretations of the modeled structure, the LAB does not contain significant amounts of interconnected partial melt. To determine the conductivity mechanisms operative at the LAB we compared a 1-D profile averaged from our preferred 2-D model to laboratory conductivity data of anhydrous and hydrous olivine and interpretations of the electrical structure from other oceanic settings.

Results from our analysis advocate for three separate interpretations. The first interpretation is a purely thermal explanation for the observed NoMelt conductivity where the mantle adiabat has a gradient of 0.5°C/km and a potential temperature of 1374°C. The intersection of the adiabat and the plate geotherm constrained by bathymetric data is at 86 km and 1412°C. If instead a lower adiabatic thermal gradient of 0.3°C/km is preferred, in keeping with other constraints on mantle properties [e.g., *Turcotte and Schubert*, 2002], the potential temperature of the mantle increases to 1386°C but plate thickness and basal temperature remains the

same. However, this choice of adiabat underpredicts asthenospheric conductivity assuming a dry olivine composition, suggesting that another mechanism is needed to explain the observed NoMelt mantle conductivity. We suggest that a small amount of H_2O dissolved in olivine is a viable explanation, although the range of asthenospheric bulk H_2O contents is highly dependent on the choice of conductive hydrous olivine model chosen, as well as the choice of dry olivine conductivity model. We estimate bulk mantle H_2O contents between 25 and 400 ppm at 300 km depth, broadly consistent with petrologic constraints on mantle H_2O contents. These concentrations of H_2O are insufficient, by themselves, to lower the mantle solidus for melting to occur.

We do not see strong evidence in the NoMelt electrical structure for melting of the asthenosphere and our observed profile does not appear to cross the anhydrous or hydrous solidi. However, we cannot rule out that the presence of CO_2 in the mantle could lower the mantle solidus sufficiently to allow for mantle melting. The amount of CO_2 in the mantle and the effects of CO_2 content on the mantle solidus are not well constrained, but if it is assumed that 100 ppm CO_2 is enough to initiate melting then small amounts of melt could be present throughout the NoMelt lower lithosphere and asthenosphere. Only trace amounts of melt ($<$0.1 vol %) are necessary to explain our observed conductivity at LAB depths.

Acknowledgments

We would like to thank Nick Schmerr and two anonymous reviewers for providing comments that significantly improved our manuscript. The results presented in this paper rely on data collected at magnetic observatories. We thank the national institutes that support them and INTERMAGNET for promoting high standards of magnetic observatory practice (www.intermagnet.org). Magnetotelluric data from the NoMelt experiment will be made freely accessible through the IRIS MT repository (http://ds.iris.edu/spud/emtf). Funding for the NoMELT experiment was provided by the National Science Foundation through the following grant numbers: OCE-0927172, OCE-0928270, OCE-1459649, and OCE-0928663. We would like to thank Chris Judge for his assistance in mobilizing the MT instruments and with their deployment and recovery at sea.

References

Anderson, D. L., and C. Sammis (1970), Partial melting in the upper mantle, *Phys. Earth Planet. Inter.*, *3*, 41–50.

Anderson, D. L., and H. Spetzler (1970), Partial melting and the low-velocity zone, *Phys. Earth Planet. Inter.*, *4*, 62–64.

Ardia, P., M. M. Hirschmann, A. C. Withers, and T. J. Tenner (2012), H_2O storage capacity of olivine at 5–8 GPa and consequences for dehydration partial melting of the upper mantle, *Earth Planet. Sci. Lett.*, *345–348*, 104–116.

Baba, K., and A. D. Chave (2005), Correction of seafloor magnetotelluric data for topographic effects during inversion, *J. Geophys. Res.*, *110*, B12105, doi:10.1029/2004JB003463.

Baba, K., A. D. Chave, R. L. Evans, G. Hirth, and R. L. Mackie (2006), Mantle dynamics beneath the East Pacific Rise at 17°S: Insights from the Mantle Electromagnetic and Tomography (MELT) experiment, *J. Geophys. Res.*, *111*, B02101, doi:10.1029/2004JB003598.

Baba, K., H. Utada, T. Goto, T. Kasaya, H. Shimizu, and N. Tada (2010), Electrical conductivity imagine of the Philippine Sea upper mantle using seafloor magnetotelluric data, *Phys. Earth Planet. Inter.*, *183*, 44–62.

Bagley, B., and J. Revenaugh (2008), Upper mantle seismic shear discontinuities of the Pacific, *J. Geophys. Res.*, *113*, B12301, doi:10.1029/2008JB005692.

Beghein, C., K. Yuan, N. Schmerr, and Z. Xing (2014), Changes in seismic anisotropy shed light on the nature of the Gutenberg Discontinuity, *Science*, *343*, 1237–1240.

Bunge, H. P., M. A. Richards, and J. R. Baumgardner (1996), Effect of depth-dependent viscosity on the planform of mantle convection, *Nature*, *379*, 436–438.

Chave, A. D., and D. J. Thomson (2003), A bounded influence regression estimator based on the statistics of the hat matrix, *J. R. Stat. Soc., Ser. C*, *52*, 307–322.

Chave, A. D., and D. J. Thomson (2004), Bounded influence magnetotelluric response function estimation, *Geophys. J. Int.*, *157*, 988–1006.

Collins, J. A., F. L. Vernon, J. A. Orcutt, and R. A. Stephen (2002), Upper mantle structure beneath the Hawaiian swell: Constraints from the ocean seismic network pilot experiment, *Geophys. Res. Lett.*, *29*(11), 1522, doi:10.1029/2001GL013302.

Constable, S. (2006), SEO3: A new model of olivine electrical conductivity, *Geophys. J. Int.*, *166*, 435–437.

Constable, S., T. J. Shankland, and A. Duba (1992), The electrical conductivity of an isotropic olivine mantle, *J. Geophys. Res.*, *97*, 3397–3404, doi:10.1029/91JB02453.

Crosby, A. G., D. McKenzie, and J. G. Sclater (2006), The relationship between depth, age and gravity in the oceans, *Geophys. J. Int.*, *166*, 553–573, doi:10.1111/j.1365-246X.2006.03015x.

Dai, L., and S. Karato (2009), Electrical conductivity of wadsleyite at high temperatures and high pressures, *Earth Planet. Sci. Lett.*, *287*, 277–283.

Dai, L., and S. Karato (2014), High and highly anisotropic electrical conductivity of the asthenosphere due to hydrogen diffusion in olivine, *Earth Planet. Sci. Lett.*, *408*, 79–86, doi:10.1016/j.epsl.2014.10.003.

Dasgupta, R., and M. M. Hirschmann (2006), Melting in the Earth's deep upper mantle caused by carbon dioxide, *Nature*, *440*, 659–662, doi:10.1038/nature04612.

Dasgupta, R., A. Mallik, K. Tsuno, A. C. Withers, G. Hirth, and M. M. Hirschmann (2013), Carbon-dioxide-rich silicate melt in the Earth's upper mantle, *Nature*, *493*, 211–215, doi:10.1038/nature11731.

Eaton, D. W., F. Darbyshire, R. L. Evans, H. Grütter, A. Jones, and X. Yuan (2009), The elusive lithosphere-asthenosphere boundary (LAB) beneath cratons, *Lithos*, *109*, 1–22, doi:10.1016/j.lithos.2008.05.009.

Evans, R. L. (2012), Chapter 3: Earth's electromagnetic environment. Part 1: Conductivity of earth materials, in *The Magnetotelluric Method: Theory and Practice*, edited by A. D. Chave and A. G. Jones, Cambridge Univ. Press, Cambridge, U. K.

Evans, R. L., G. Hirth, K. Baba, D. Forsyth, A. D. Chave, and R. Mackie (2005), Geophysical evidence from the MELT area for compositional controls on oceanic plates, *Nature*, *437*, 249–252.

Evans, R. L., D. Lizarralde, J. A. Collins, J. Elsenbeck, E. Tursack, G. Hirth, J. B. Gaherty, A. Pommier, K. Baba, and T. Matsuno (2011), Electromagnetic constraints on the structure of the oceanic upper mantle: Consistencies and inconsistencies with other observations, Abstract DI34B-03 presented at 2011 Fall Meeting, AGU, San Francisco, Calif., 5–9 Dec.

Fei, H., M. Wiedenbeck, D., Yamazake, and T. Katsura (2013), Small effect of water on upper-mantle rheology based on silicon self-diffusion coefficients, *Nature*, *498*, 213–215.

Gaherty, J. B., T. H. Jordan, and L. S. Gee (1996), Seismic structure of the upper mantle in a central Pacific corridor, *J. Geophys. Res.*, *101*, 22,291–22,309, doi:10.1029/96JB01882.

Gaherty, J. B., D. Lizarralde, J. A. Collins, G. Hirth, and S. Kim (2004), Mantle deformation during slow seafloor spreading constrained by observations of seismic anisotropy in the western Atlantic, *Earth Planet. Sci. Lett.*, *288*(3), 255–265.

Gaillard, F., M. Malki, G. Iacono-Marziano, M. Pichavant, and B. Scaillet (2008), Carbonatite melts and electrical conductivity in the asthenosphere, *Science*, *322*, 1363–1365.
Gardes, E., F. Gaillard, and P. Tarits (2014), Toward a unified hydrous olivine electrical conductivity law, *Geochem. Geophys. Geosyst.*, *15*, 4984–5000, doi:10.1002/2014GC005496.
Gu, Y. J., A. L. Lerner-Lam, A. M. Dziewonski, and G. Ekstrom (2005), Deep structure and seismic anisotropy beneath the East Pacific Rise, *Earth Planet. Sci. Lett.*, *232*, 259–272.
Hashin, Z., and S. Shtrikman (1962), A variational approach to the theory of effective magnetic permeability of multiphase materials, *J. Appl. Phys.*, *33*, 3125–3131.
Hirschmann, M. M. (2000), Mantle solidus: Experimental constraints and the effects of peridotite composition, *Geochem. Geophys. Geosyst.*, *1*(10), 1042, doi:10.1029/2000GC000070.
Hirschmann, M. M. (2010), Partial melt in the oceanic low velocity zone, *Phys. Earth Planet. Inter.*, *179*, 60–71.
Hirschmann, M. M., and R. Dasgupta (2009), The H/C ratios of Earth's near-surface and deep reservoirs, and consequences for deep Earth volatile cycles, *Chem. Geol.*, *262*, 4–16.
Hirschmann, M. M., T. Tenner, C. Aubaud, and A. C. Withers (2009), Dehydration melting of nominally anhydrous mantle: The primacy of partitioning, *Phys. Earth Planet. Inter.*, *176*, 54–68.
Hirth, G., and D. L. Kohlstedt (1996), Water in the oceanic upper mantle: Implications for rheology, melt extraction and the evolution of the lithosphere, *Earth Planet. Lett.*, *144*, 93–108.
Hoink, T., and A. Lenardic (2008), Three-dimensional mantle convection simulations with a low-viscosity asthenosphere and the relationship between heat flow and the horizontal length scale of convection, *Geophys. Res. Lett.*, *35*, L10304, doi:10.1029/2008GL033854.
Jones, A. G., J. Fullea, R. L. Evans, and M. R. Muller (2012), Water in cratonic lithosphere: Calibrating laboratory-determined models of electrical conductivity of mantle minerals using geophysical and petrological observations, *Geochem. Geophys. Geosyst.*, *13*, Q06010, doi:10.1029/2012GC004055.
Karato, S. (2006), Remote sensing of hydrogen in Earth's mantle, *Rev. Mineral. Geochem.*, *62*, 343–375.
Karato, S. (2012), On the origin of the asthenosphere, *Earth Planet. Sci. Lett.*, *321–322*, 95–103.
Karato, S. (2013), Theory of isotope diffusion in a material with multiple species and its implications for hydrogen-enhanced electrical conductivity in olivine, *Phys. Earth Planet. Inter.*, *219*, 49–54.
Karato, S., and H. Jung (1998), Water, partial melting and the origin of the seismic low velocity and high attenuation zone in the upper mantle, *Earth Planet. Sci. Lett.*, *157*, 193–207.
Katsura, T., A. Yoneda, D. Yamazaki, T. Yoshino, and E. Ito (2010), Adiabatic temperature profile in the mantle, *Phys. Earth Planet. Inter.*, *183*, 212–218.
Katz, R. F., M. Spiegelman, and C. H. Langmuir (2003), A new parameterization of hydrous mantle melting, *Geochem. Geophys. Geosyst.*, *4*(9), 1073, doi:10.1029/2002GC000433.
Kawakatsu, H., P. Kumar, Y. Takei, M. Shinohara, T. Kanazawa, E. Araki, and K. Suyehiro (2009), Seismic evidence for sharp lithosphere-asthenosphere boundaries of oceanic plates, *Science*, *324*, 499–502.
Kohlstedt, D. L., and S. J. Mackwell (1998), Diffusion of hydrogen and intrinsic point defects in olivine, *Z. Phys. Chem.*, *207*, 147–162.
Lambert, I. B., and P. J. Wyllie (1970), Low-velocity zone of the Earth's mantle: Incipient melting caused by water, *Science*, *169*, 764–766.
Mackwell, S. J., and D. L. Kohlstedt (1990), Diffusion of hydrogen in olivine: Implications for water in the mantle, *J. Geophys. Res.*, *95*, 5079–5088, doi:10.1029/JB095iB04p05079.
Matsuno, T., et al. (2010), Upper mantle electrical resistivity structure beneath the central Mariana subduction system, *Geochem. Geophys. Geosyst.*, *11*, Q09003, doi:10.1029/2010GC003101.
McKenzie, D., and M. Bickle (1988), The volume and composition of melt generated by extension of the lithosphere, *J. Petrol.*, *29*(3), 625–679.
Michael, P. J. (1988), The concentration, behavior and storage of H_2O in the suboceanic upper mantle: Implications for mantle metasomatism, *Geochim. Cosmochim. Acta*, *52*, 555–566.
Minarik, W. G., and E. B. Watson (1995), Interconnectivity of carbonate melt at low melt fraction, *Earth Planet. Sci. Lett.*, *133*, 423–437.
Montagner, J. P., and T. Tanimoto (1991), Global upper mantle tomography of seismic velocities and anisotropies, *J. Geophys. Res. Solid Earth*, *96*, 20337–20351.
Naif, S., K. Key, S. Constable, and R. L. Evans (2013), Melt-rich channel observed at the lithosphere-asthenosphere boundary, *Nature*, *495*, 356–359.
Nettles, M., and A. M. Dziewonski (2008), Radially anisotropic shear velocity structure of teh upper mantle globally and beneath North America, *J. Geophys. Res.*, *113*, doi:10.1029/2006jb004819.
Ni, H., H. Keppler, and H. Behrens (2011), Electrical conductivity of hydrous basaltic melts: Implications for partial melting in the upper mantle, *Contrib. Mineral. Petrol.*, *162*, 637–650.
Nishimura, C. E., and D. W. Forsyth (1989), The anisotropic structure of the upper mantle in the Pacific, *Geophys. J.*, *96*, 203–229.
O'Leary, J. A., G. A. Gaetani, and E. H. Hauri (2010), The effect of tetrahedral Al^{3+} on the partitioning of water between clinopyroxene and silicate melt, *Earth Planet. Sci. Lett.*, *297*, 111–120.
Olugboji, T. M., S. Karato, and J. Park (2013), Structures of the oceanic lithosphere-asthenosphere boundary: Mineral-physics modeling and seismological signatures, *Geochem. Geophys. Geosyst.*, *14*, 880–901, doi:10.1002/ggge.20086.
Parsons, B., and J. G. Sclater (1977), An analysis of the variation of ocean floor bathymetry and heat flow with age, *J. Geophys. Res.*, *82*, 803–827, doi:10.1029/JB082i005p00803.
Morgan, J. P. (1997), The generation of a compositional lithosphere by mid-ocean ridge melting and its effect on subsequent off-axis hotspot upwelling and melting, *Earth Planet. Sci. Lett.*, *146*(1), 213–232.
Plomerová, J., D. Kouba, and V. Babuška (2002), Mapping the lithosphere-asthenosphere boundary through changes in surface-wave anisotropy, *Tectonophysics*, *358*, 175–185.
Poe, B. T., C. Romano, F. Nestola, and J. R. Smyth (2010), Electrical conductivity anisotropy of dry and hydrous olivine at 8 GPa, *Phys. Earth Planet. Inter.*, *181*, 103–111.
Pommier, A., and E. J. Garnero (2014), Petrology-based modeling of mantle melt electrical conductivity and joint interpretation of electromagnetic and seismic results, *J. Geophys. Res. Solid Earth*, *119*, 4001–4016, doi:10.1002/2013JB010449.
Pommier, A., F. Gaillard, M. Pichavant, and B. Scaillet (2008), Laboratory measurements of electrical conductivities of hydrous and dry Mount Vesuvius melts under pressure, *J. Geophys. Res.*, *113*, B05205, doi:10.1029/2007JB005269.
Priestley, K., and D. McKenzie (2006), The thermal structure of the lithosphere from shear wave velocities, *Earth Planet. Sci. Lett.*, *244*, 285–301.

Raitt, R. W., G. G. Shor Jr., T. J. G. Francis, and G. B. Morris (1969), Anisotropy of the Pacific upper mantle, *J. Geophys. Res.*, *74*(12), 3095–3109.
Revenaugh, J., and T. H. Jordan (1991), Mantle layering from ScS reverberations. 1: Waveform inversion of zeroth-order reverberations, *J. Geophys. Res.*, *96*, 19,749–19,762, doi:10.1029/91JB01659.
Richards, M. A., W. S. Yang, J. R. Baumgardner, and H. P. Bunge (2002), Role of a low-viscosity zone in stabilizing place tectonics: Implications for comparative terrestrial planetology, *Geochem. Geophys. Geosyst.*, *2*(8), 1026, doi:10.1029/2000GC000115.
Riley, G. N., D. L. Kohlstedt, and P. M. Richter (1990), Melt migration in a silicate liquid-olivine system: An experimental test of compaction theory, *Geophys. Res. Lett.*, *17*, 2101–2104, doi:10.1029/GL017i012p02101.
Ritzwoller, M. H., N. M. Shapiro, and S. Zhong (2004), Cooling history of the Pacific lithosphere, *Earth Planet. Sci. Lett.*, *226*, 69–84.
Roberts, J. J., and J. A. Tyburczy (1999), Partial-melt electrical conductivity: Influence of melt composition, *J. Geophys. Res.*, *104*, 7055–7065, doi:10.1029/1998JB900111.
Rodi, W., and R. L. Mackie (2001), Nonlinear conjugate gradients algorithm for 2-D magnetotelluric inversion, *Geophysics*, *66*, 174–187.
Rychert, C. A., and P. M. Shearer (2009), A global view of the lithosphere-asthenosphere boundary, *Science*, *324*(5926), 495–498, doi: 10.1126/science.1169754.
Rychert, C. A., and P. M. Shearer (2011), Imaging the lithosphere-ashtenosphere boundary beneath the Pacific using SS waveform modeling, *J. Geophys. Res.*, *116*, B07307, doi:10.1029/2010JB008070.
Rychert, C. A., N. Schmerr, and N. Harmon (2012), The Pacific lithosphere-asthenosphere boundary: Seismic imaging and anisotropic constraints from SS waveforms, *Geochem. Geophys. Geosyst.*, *13*, Q0AK10, doi:10.1029/2012GC004194.
Saal, A. E., E. H. Hauri, C. H. Langmuir, and M. R. Perfit (2002), Vapour undersaturation in primitive mid-ocean-ridge basalt and the volatile content of Earth's upper mantle, *Nature*, *419*, 451–455.
Schmeling, H. (1986), Numerical models on the influence of partial melt on elastic, anelastic and electrical properties of rocks. Part II: Electrical conductivity, *Phys. Earth Planet. Inter.*, *43*, 123–136.
Schmerr, N. (2012), The Gutenberg discontinuity: Melt at the lithosphere-asthenosphere boundary, *Science*, *335*, 1480–1483.
Shankland, T. J., and H. S. Waff (1977), Partial melting and electrical conductivity anomalies in the upper mantle, *J. Geophys. Res.*, *82*, 5409–5417.
Sifre, D., E. Gardes, M. Massuyeau, L. Hashim, S. Hier-Majumder, and F. Gaillard (2014), Electrical conductivity during incipient melting in the oceanic low-velocity zone, *Nature*, *509*, 81–85.
Simons, K., J. Dixon, J.-G. Schilling, R. Kingsley, and R. Poreda (2002), Vapour undersaturation in primitive mid-ocean ridge basalt and the volatile content of Earth's upper mantle, *Nature*, *419*, 451–455.
Stein, C., and S. Stein (1992), A model for the global variation in oceanic depth and heat flow with lithospheric age, *Nature*, *359*, 123–129.
Stixrude, L., and C. Lithgow-Bertelloni (2005), Mineralogy and elasticity of the oceanic upper mantle: Origin of the low-velocity zone, *J. Geophys. Res.*, *110*, B03204, doi:10.1029/2004JB002965.
Tan, Y., and D. Helmberger (2007), A new method for determining small earthquake source parameters using short-period P waves, *Seismol. Soc. Am.*, *97*, 1176–1195, doi:10.1785/0120060251.
ten Grotenhuis, S. M., M. R. Drury, C. J. Spiers, and C. J. Peach (2005), Melt distribution in olivine rocks based on electrical conductivity measurements, *J. Geophys. Res.*, *110*, B12201, doi:10.1029/2004JB003462.
Toffelmier, D. A., and J. A. Tyburczy (2007), Electromagnetic detection of a 410-km-deep melt layer in the southwestern United States, *Nature*, *447*, 991–994.
Toramaru, A., and N. Fujii (1986), Connectivity of melt phase in a partially molten peridotite, *J. Geophys. Res.*, *91*, 9239–9252, doi:10.1029/JB091iB09p09239.
Turcotte, D. L., and G. Schubert (2002), *Geodynamics*, 2nd ed., Cambridge Univ. Press, Cambridge, U. K.
Utada, H., and K. Baba (2014), Estimating the electrical conductivity of the melt phase of a partially molten asthenosphere from seafloor magnetotelluric sounding data, *Phys. Earth Planet. Inter.*, *227*, 41–47.
Wang, D., M. Mookherjee, Y. Xu, and S. Karato (2006), The effect of water on the electrical conductivity of olivine, *Nature*, *443*, 977–980.
Wannamaker, P. E., J. R. Booker, A. G. Jones, A. D. Chave, J. H. Filloux, H. S. Waff, and L. K. Law (1989), Resistivity cross section through the Juan de Fuca subduction system and its tectonic implications, *J. Geophys. Res.*, *94*, 14,127–14,144, doi:10.1029/JB094iB10p14127.
Wolfe, C. J., and S. C. Solomon (1998), Shear-wave splitting and implications for mantle flow beneath the MELT region of the East Pacific Rise, *Science*, *280*, 1230–1232.
Workman, R. K., and S. R. Hart (2005), Major and trace element composition of the depleted MORB mantle (DMM), *Earth Planet. Sci. Lett.*, *231*, 53–72.
Xu, Y., T. J. Shankland, and A. G. Duba (2000), Pressure effect on electrical conductivity of mantle olivine, *Phys. Earth Planet. Int.*, *118*(1), 149–161.
Yang, X. (2012), Orientation-related electrical conductivity of hydrous olivine, clinopyroxene and plagioclase and implications for the structure of the lower continental crust and uppermost mantle, *Earth Planet. Sci. Lett.*, *317–318*, 241–250.
Yang, X., D. Liu, and Q. Xia (2014), CO_2-induced small water solubility in olivine and implications for properties of the shallow mantle, *Earth Planet. Sci. Lett.*, *403*, 37–47.
Yoshino, T., T. Matsuzaki, S. Yamashita, and T. Katsura, (2006), Hydrous olivine unable to account for conductivity anomaly at the top of the asthenosphere, *Nature*, *443*(7114), 973–976.
Yoshino, T., T. Matsuzaki, A. Shatskiy, and T. Katsura (2009), The effect of water on the electrical conductivity of olivine aggregates and its implications for the electrical structure of the upper mantle, *Earth Planet. Sci. Lett.*, *288*, 291–300.
Yoshino, T., M. Laumonier, E. McIsaac, and T. Katsura (2010), Electrical conductivity of basaltic and carbonatite melt-bearing peridotites at high pressures: Implications for melt distribution and melt fraction in the upper mantle, *Earth Planet. Sci. Lett.*, *295*, 593–602.
Yoshino, T., E. McIsaac, M. Laumonier, and T. Katsura (2012), Electrical conductivity of partial molten carbonate peridotite, *Phys. Earth Planet. Inter.*, *194–195*, 1–9.
Zhu, W., G. A. Gaetani, F. Fusseis, L. G. J. Montesi, and F. De Carlo (2011), Microtomography of partially molten rocks: Three-Dimensional melt distribution in mantle peridotite, *Science*, *332*, 88–91.